Coherent Wave–Zonal Mean Flow Interactions in the Troposphere

WILLIAM J. RANDEL

National Center for Atmospheric Research, Boulder, Colorado*

(Manuscript received 10 February 1989, in final form 25 August 1989)

ABSTRACT

Spatial structure and temporal evolution of synoptic time scale variations of the tropospheric zonal mean flow are studied by extensive cross-correlation analyses, and the degree to which observations agree with two-dimensional, adiabatic theory is determined. Observational data from seven years of operational daily global analyses are studied, along with data from the NCAR general circulation model.

Observed zonal mean zonal wind and temperature tendencies are compared with analyzed adiabatic forcing terms. Although significant correlations are found throughout the extratropics, there are significant equation residuals in both operational analyses and model data. Model momentum residuals result from calculational inaccuracies (interpolation to pressure surfaces and spectral aliasing of nonlinear terms) and biases introduced by once daily sampling; diabatic terms are also important for the daily thermodynamic balance.

Coherent wave–zonal mean flow interactions are revealed via cross-correlation analyses, including fluctuations in zonal mean temperature, three-dimensional winds, and quadratic wave quantities. Equatorward propagating wavelike patterns in the meridional plane are observed for both zonal wind and temperature tendencies. These patterns result from midlatitude baroclinic-wave life cycles, and the signatures associated with wave growth and decay are revealed with novel detail. New observed features of baroclinic wave life cycles shown here include coherent fluctuations of the extratropical mean meridional circulation (Ferrel cells), and equatorward propagation of midlatitude wave activity (Rossby-wave radiation) as far as the equator.

An individual case study is presented to show the variability associated with a particular event.

1. Introduction

The theory of wave–mean flow interactions applied to the zonal mean atmosphere has recently received considerable attention. Edmon et al. (1980) described the motivation behind using the transformed Eulerian-mean (TEM) formalism for describing wave–mean flow interactions, and pioneered its use in analyzing the time-mean atmospheric structure. Trenberth (1987) and Pfeffer (1987) used recent observational data to study the influence of waves on the time-mean tropospheric flow, both papers comparing the TEM with traditional Eulerian-mean diagnostics. The role of transcience in the wave–mean flow interaction problem has received considerably less attention, particularly for observational studies. Edmon et al. (1980) detailed various stages of idealized baroclinic wave life cycles (from the model results of Simmons and Hoskins 1978) by Eliassen–Palm (EP) flux diagnostics, and further detail was described in Hoskins (1983). Randel and Stanford (1985) described the evolution of a particularly clear life cycle observed during the SH summer using similar diagnostics. However, these studies focused primarily on the evolving wave characteristics rather than the detailed momentum and thermodynamic balances throughout the wave life cycles.

The purpose of this study is to provide a comprehensive analysis of wave–zonal mean flow variations in the troposphere from observed data. Seven years of daily operational analyses are examined, along with data from a general circulation model (GCM). Two main questions are addressed here:

1) How well does the zonally averaged variability (on synoptic time scales) evident in current operational analyses (and GCM data) agree with zonal mean, adiabatic theory? This is answered by comparing observed zonal momentum and thermodynamic tendencies to adiabatic forcing terms. Although there are strong contemporaneous cross-correlations, there are relatively large equation residuals in both analyzed and model data. The cause of the model residuals is diagnosed and discussed below.

2) What is the structure and evolution of coherent wave–mean flow variations that repeatedly occur in the data? This is studied by extensive cross correlation analyses. The results show coherent, propagating wavelike variations in the meridional plane for both zonal mean zonal wind and temperature tendencies. These patterns result from the growth and decay of midlatitude baroclinic waves. The correlation analyses reveal the structure and evolution of the life cycles with novel detail. The ubiquitous nature of the life cycles is attested to by their similar character in all seasons and both hemispheres, along with their nearly identical characteristics in GCM results.

* The National Center for Atmospheric Research is sponsored by the National Science Foundation.

Corresponding author address: Dr. William Randel, NCAR, P.O. Box 3000, Boulder, CO 80307-3000.

a. Theory

The zonal mean equations analyzed in this study are based on the transformed Eulerian-mean (TEM) formalism introduced in Andrews and McIntyre (1976) and Boyd (1976). These equations have been subsequently discussed by Edmon et al. (1980), Dunkerton et al. (1981), Hoskins (1983), and Trenberth (1987), among others. The zonal mean zonal wind and temperature tendency equations in the TEM formalism are written as

$$\frac{\partial \bar{u}}{\partial t} - (\hat{f}\overline{v^*} + D_F) = R_u \tag{1}$$

$$\frac{\partial \bar{T}}{\partial t} + S\overline{w^*} = R_T. \tag{2}$$

These equations (and those following) are the quasi-geostrophic approximations to the full (primitive) equations given in Dunkerton et al. (1981), but retaining the vorticity of the zonal mean wind [via $\hat{f} = 2\Omega \sin\phi - (1/a\cos\phi)\partial(\bar{u}\cos\phi)/\partial\phi$]. The results to be shown here were insensitive to inclusion of other ageostrophic terms. Here S is a (latitude–height dependent) measure of the static stability $S = (k\bar{T} + (\partial\bar{T}/\partial z))$. These equations are written in latitude (ϕ) – log-pressure (z) coordinates, where $z = \ln(p_0/p)$, with $p_0 = 1000$ mb. Overbars denote zonal means and primes deviations therefrom. R_u and R_T are the respective equation residuals in Eqs. (1)–(2), and can result from neglected effects (unresolved scales of motion, vertical advections, friction, diabatic forcings) and/or inadequacy of the database.

In Eq. (1) D_F is the scaled divergence of the Eliassen–Palm (EP) flux vector $\vec{F}$ (also called the wave driving):

$$D_F = \frac{1}{a\cos\phi \cdot \rho_s}\left[\frac{1}{a\cos\phi}\frac{\partial}{\partial\phi}F_\phi + \frac{\partial}{\partial z}F_z\right] \tag{3a}$$

where

$$\vec{F} = \begin{pmatrix} F_\phi \\ F_z \end{pmatrix} = a\cos\phi\rho_s \begin{pmatrix} -\overline{u'v'} \\ \hat{f}\dfrac{\overline{v'T'}}{S} \end{pmatrix} \tag{3b}$$

and $\overline{v^*}$ and $\overline{w^*}$ are components of the "residual" meridional circulation defined as

$$\overline{v^*} = \bar{v} - \frac{1}{\rho_s}\frac{\partial}{\partial z}\left(\rho_s\frac{\overline{v'T'}}{S}\right) \tag{4a}$$

$$\overline{w^*} = \bar{w} + \frac{1}{a\cos\phi}\frac{\partial}{\partial\phi}\left(\cos\phi\,\frac{\overline{v'T'}}{S}\right). \tag{4b}$$

Here $\rho_s = \rho_0 e^{-z}$ is the basic state density profile, with $\rho_0 = 1.27$ kg m^{-3}.

2. Data and analyses

a. Observed data

Observational results are based on zonal mean cross-sections from operational three-dimensional wind and temperature analyses produced by the European Centre for Medium Range Weather Forecasts (ECMWF). Daily data are studied for 1980–86. Trenberth and Olson (1988) have extensively discussed the quality of these data, and have noted apparently spurious changes in the analyzed zonal-mean meridional and vertical winds in the tropics (Hadley cell), as the operational schemes have been modified over 1979–86. The calculations here include analyzed mean meridional velocities [Eqs. (4a) and (4b)], but focus mainly on extratropics (polewards of 20°); Trenberth and Olson's results show less spurious variability and suggest more reliable analyses away from the tropics.

The data studied here have been spectrally truncated at rhomboidal wavenumber 15, corresponding to a resolution near 4.5° lat × 7.5° long. Data are available on pressure levels of 1000, 850, 700, 500, 300, 200, and 100 mb. Time and meridional finite differences are calculated using a five point +0.095, −0.690, 0., +0.690, and −0.095 centered formulation; this provides a more accurate approximation to a continuous derivative for relatively short scale features (of order four grid spaces) than a three point −0.5, 0, and +0.5 approximation. Vertical derivatives are calculated by differencing between adjacent available pressure levels, followed by linear interpolation (in log pressure) back to the standard levels.

b. GCM data

Data from a GCM are analyzed here in addition to the observations. The main advantage of using data from a GCM is that the instantaneously sampled values exactly satisfy the governing equations of the model, so that the data are "perfectly" sampled. On the other hand, no GCM is a perfect model of the atmosphere, and comparisons must be made in light of the respective differing climates. In particular, the parameterized physical processes included in the model may have a different influence than diabatic forcing in the atmosphere; this can be particularly important in the thermodynamic budget.

The model analyzed here is the NCAR Community Climate Model denoted CCM1; it is integrated with horizontal spectral truncation at rhomboidal wave 15 (R15) and twelve vertical σ-levels. Individual fields are interpolated to pressure surfaces coincident with the ECMWF analyses prior to further calculations. Seven years of daily sampled model data are analyzed here, and all calculations are made in an identical manner to those for the observed data. An extensive comparison of the climate of CCM1 with ECMWF analyses is given in Randel and Williamson (1989).

c. Data analyses

Cross-correlation analyses are used extensively here. Correlation statistics are calculated from 90-day time series centered on each season (1 December–28 February, 1 March–29 May, etc.), and averaged over the seven years of data. Significance levels for the correlations here are estimated as in Lau and Chan [1983, their Eq. (A8)]. Using three days as a conservative estimate of the e-folding time scale for all the variables here (i.e., the time lag at which the respective autocorrelations fall to a value of $1/e$), and using 630 (90×7) total observations, an estimate of the standard deviation for the seasonal correlation coefficient between two uncorrelated variables is approximately 0.08; 5% and 1% significance levels for the seasonal correlations here are then approximately 0.16 and 0.21, respectively. The wave–mean flow cross-correlations in section 5 are four seasonal averages, for which the corresponding significance levels are narrowed by a factor of 2 (near 0.08 and 0.105). These numbers provide only a rough guide—the main focus in the correlation analyses are the spatial structures in the meridional plane, and temporal evolution of the correlation patterns.

When analyzing variations of zonal mean quantities, it is important to be aware that variance will tend to increase with latitude due solely to the spherical geometry of the earth. North et al. (1982) suggest that the influence of the geometrical increase can be assessed by comparing the variance of the zonal means with the zonal mean of the (longitudinal) grid point variance values. North et al. (1982) show that the increase of variance with latitude for idealized statistics (and also for observed geopotential height fluctuations) follows an approximate inverse cosine of latitude dependence [their Eq. (8)]; similar dependence (not shown) is observed in high latitudes for the data studied here. To alleviate this dependence, *all subsequent maps of zonal mean daily standard deviations are multiplied by the square root of the cosine of latitude.*

3. Equation balances for daily variability of the zonal mean flow

a. Observed data

This section analyzes daily variations in the separate terms of Eqs. (1) and (2) by presenting meridional cross sections of the respective daily standard deviations, and the degree to which the equations balance on a daily basis is evaluated by comparison with the respective rms equation residuals. Details of the statistics for March–April–May are studied here; similar results are found in all other seasons.

Figure 1 shows daily standard deviation maps for the observed time tendency ($\partial\bar{u}/\partial t$) and forcing term ($\hat{f}\overline{v^*} + D_F$) in Eq. (1); the rms equation residual is simply the rms daily sum of both terms. In the time

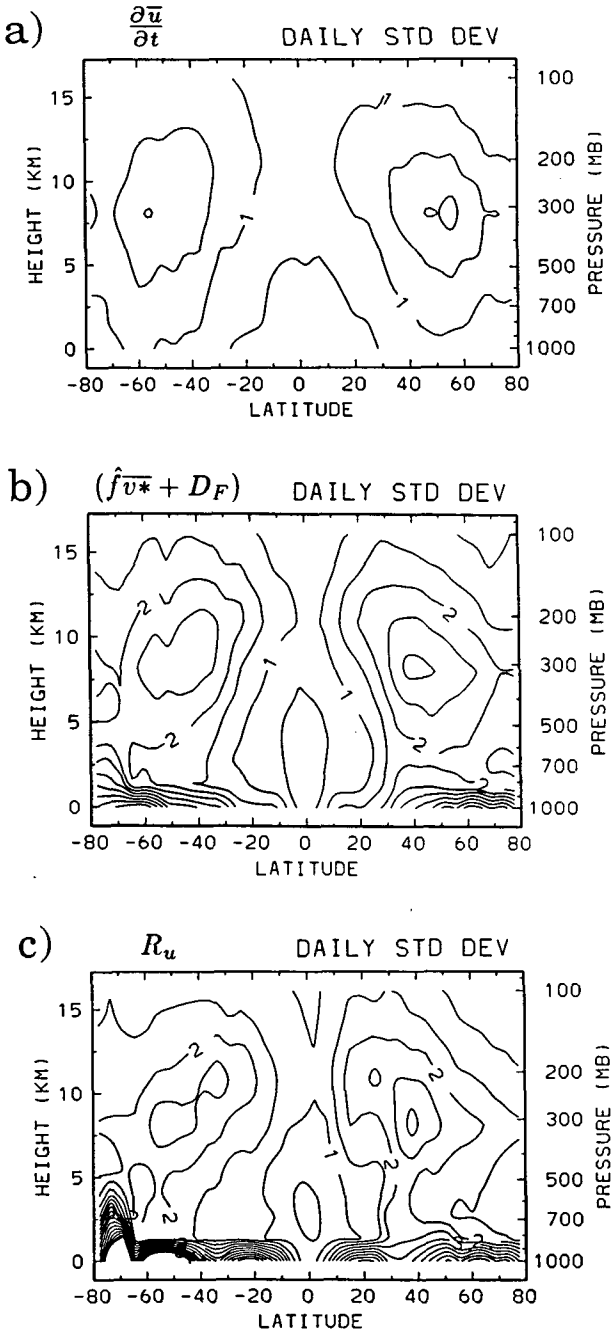

FIG. 1. Observed daily standard deviations of individual terms in the zonal mean zonal wind tendency equation, Eq. (1); contours of 0.5 m s^{-1} day^{-1}.

average, the balance in Eq. (1) over most of the troposphere is between $\hat{f}\overline{v^*}$ and D_F (not shown here—see the results for the Southern Hemisphere (SH) winter in Trenberth 1987); $\partial\bar{u}/\partial t$ is negligible in the time mean, and the equation residual has maximum local values on the order of 1 m s^{-1} day^{-1} (ageostrophic terms are of order 0.5 m s^{-1} day^{-1}, but their inclusion

does *not* systematically reduce the time-mean equation residual). Daily standard deviations of all terms in Eq. (1) (Fig. 1) peak in midlatitudes in the upper troposphere (near 300 mb), with the forcing and residual also having maxima near the surface. The rms equation residual is somewhat larger than, but of the same order as, $\partial\bar{u}/\partial t$ above the lowest levels, showing that there can be little expectation of evaluating $\partial\bar{u}/\partial t$ beyond a factor of 2 on a daily basis from these data. The largest residuals are found near the surface, showing poor balance in Eq. (1) there. Temporal power spectra for these variables (not shown) exhibit maximum power for periods of order 5 to 10 days; i.e., these variance maps are for "synoptic" time scale variations.

Figure 2 shows daily standard deviation maps for terms in the zonal mean temperature tendency equation, Eq. (2). Local time mean values of $S\bar{w}^*$ in extratropics are of order 0.25°–0.50°K day^{-1}, and the convergence of vertical eddy heat flux [an ageostrophic term not included in Eq. (2)] is of this same order but does not systematically balance $S\bar{w}^*$; there is a relatively large time mean Eq. (2) residual that is presumably balanced by diabatic effects and unresolved scales. The $S\bar{w}^*$ daily standard deviations in Fig. 2b are substantially larger than those of $\partial\bar{T}/\partial t$ (Fig. 2a), and the residual variance is of the same order or larger than that of $S\bar{w}^*$, showing a rather poor quantitative agreement between $\partial\bar{T}/\partial t$ and $S\bar{w}^*$ on a daily basis. These discrepancies are particularly large above 300 mb. Inclusion of the appropriate ageostrophic terms in Eq. (2) does not reduce this large rms equation residual.

Figure 3 shows a set of meridional cross-sections illustrating the contemporaneous correlation coefficients at each position in the meridional plane between the time tendency and forcing terms in Eqs. (1) and (2); i.e., $(\partial\bar{u}/\partial t)$ versus $(\hat{f}\bar{v}^* + D_F)$ in Fig. 3a, and $(\partial\bar{T}/\partial t)$ versus $(-S\bar{w}^*)$ in Fig. 3b. In spite of Eq. (1) residuals the same size as the $\partial\bar{u}/\partial t$ variations (Fig. 1), Fig. 3a exhibits contemporaneous correlations of order 0.5 in extratropical regions everywhere above the 850 mb level; this shows that at least the sign of $\partial\bar{u}/\partial t$ can be estimated from Eq. (1). Note that the correlations in Fig. 3a are of order 0.3 even throughout the tropics. Figure 3b shows correlation values of order 0.3–0.5 between $\partial\bar{T}/\partial t$ and $-S\bar{w}^*$, polewards of 30° in both hemispheres (somewhat stronger in the Northern Hemisphere (NH)); the correlations are strongest over 850–500 mb, with secondary maxima near 200 mb. No significant correlations are observed in the tropics.

Also added in Figs. 3c and 3d are the correlations between $(\partial\bar{u}/\partial t)$ and $\hat{f}\bar{v}^*$ alone, along with $(\partial\bar{u}/\partial t)$ and D_F alone. The opposite-signed midlatitude correlations in Figs. 3c and 3d demonstrate the opposing effects of $\hat{f}\bar{v}^*$ and D_F in Eq. (1), and the dominant effect of D_F is shown by the positive correlations with $\partial\bar{u}/\partial t$. Compared to the $(\hat{f}\bar{v}^* + D_F)$ correlations (Fig. 3a), the correlations with D_F alone are reduced significantly above 200 mb and below 500 mb; this is consistent with a deepening of the effect of localized wave forcing by the residual circulation (discussed in Dunkerton et al. 1981). The positive tropical correlations in Fig. 3a are seen to be due mainly to variations in D_F, implying that horizontal momentum flux convergences (with sources in extratropics) are coherent with tropical zonal wind variations; further results to con-

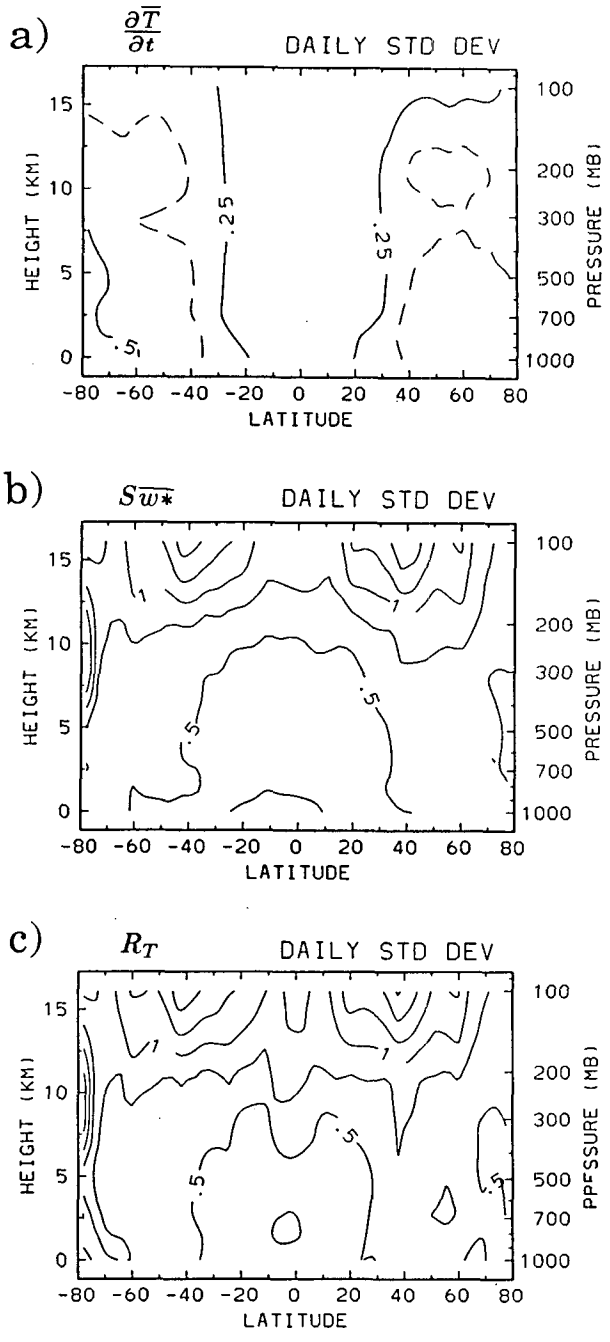

FIG. 2. As in Fig. 1, but for the zonal temperature tendency equation [Eq. (2)] daily standard deviations (contours of 0.25°K day^{-1}; dashed lines in (a) are 0.375°K day^{-1}).

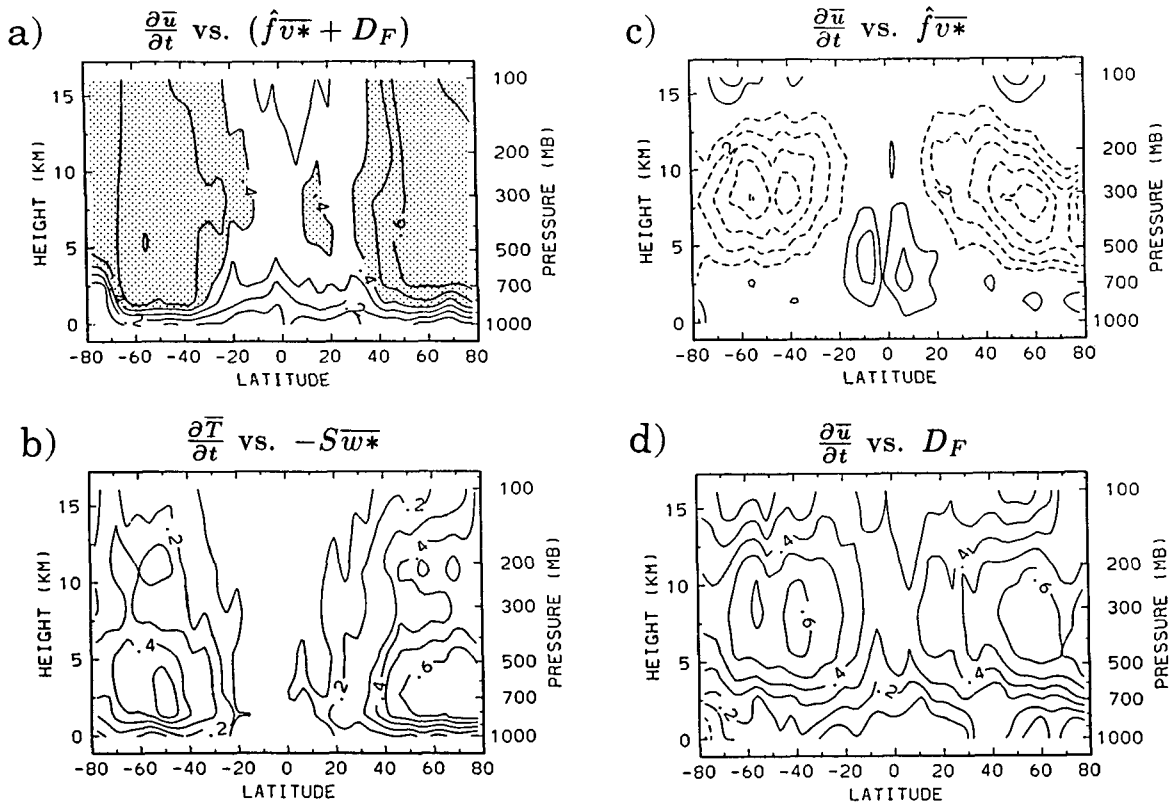

FIG. 3. Meridional cross-sections of the contemporaneous correlation coefficient between observed time tendency and forcing terms (a) $(\partial\bar{u}/\partial t)$ versus $(\hat{f}\overline{v^*} + D_F)$, (b) $\partial\bar{T}/\partial t)$ versus $(-S\overline{w^*})$, (c) $(\partial\bar{u}/\partial t)$ versus $(\hat{f}\overline{v^*})$, and (d) $(\partial\bar{u}/\partial t)$ versus (D_F). Contours of $\pm 0.1, 0.2, \ldots$.

firm this are shown in section 5a. There are also small positive correlations with $\hat{f}\overline{v^*}$ in the lower troposphere near 10°N and 10°S in Fig. 3c, showing some coherence between zonal wind and Hadley cell variations ($\hat{f}\overline{v^*}$ and $\hat{f}\bar{v}$ are nearly identical in the tropics).

Baldwin et al. (1985) have calculated statistics similar to those in Figs. 3a and 3d for a much shorter period of observations, and find values significantly less than those computed here; the reason for the lack of coherence in their study is unclear.

b. CCM1 results

The rms zonal momentum equation terms in CCM1 (not shown) exhibit spatial structures and relative magnitudes similar to the observations in Fig. 1. In particular, the momentum residual in the model is of similar size as that seen in the analyses. The model momentum residual in these calculations is caused by 1) interpolation to pressure surfaces and spectral aliasing of nonlinear terms (the nonlinear terms are truncated to R15 when calculated in the model, but not in the calculations here), and 2) the model rms $(\partial\bar{u}/\partial t)$ is substantially larger than that obtained from daily $\bar{u}$ fields; i.e., there is a large fraction of $(\partial\bar{u}/\partial t)$ variance on time scales of less than one day. Horizontal and vertical diffusions, which are the only other terms in the model momentum equation, have small effects on the daily momentum balances in the free troposphere.

The daily CCM1 thermodynamic balance is somewhat different than that seen in the ECMWF analyses. Figure 4 shows the Eq. (2) rms values for CCM1; these can be compared with the observed data in Fig. 2. The rms $\partial\bar{T}/\partial t$ patterns are similar to observations, with maxima in midlatitudes (although the model exhibits reduced upper tropospheric variability). The rms $S\overline{w^*}$ term is fundamentally different between model and observations: while the observed variance peaks in midlatitudes above 300 mb (Fig. 2b), the model fluctuations are largest in the tropics, and do not show an increase with height. The differences in extratropics are likely due to poorly analyzed upper tropospheric $\bar{w}$ and $\overline{v'T'}$ values in the observed data. In the tropics, the observed data could lack variability due to poor observations or analyses, or the model could have excessive variability due to the nature of the parameterized tropical heating (or both). The rms $\partial\bar{T}/\partial t$ equation residual in the model is nearly identical to the rms $S\overline{w^*}$ term (just as in the observed data), due to large

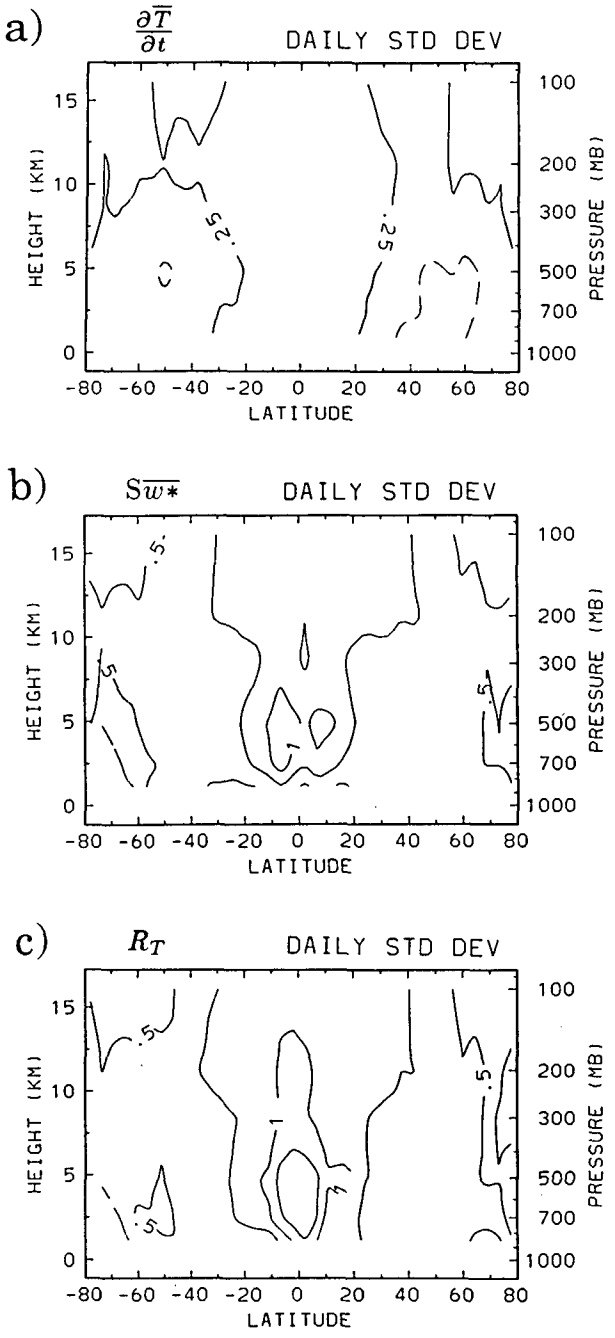

FIG. 4. Daily standard deviations of individual terms in the zonal mean temperature tendency equation, Eq. (2), for CCM1 data. Contours as in Fig. 2. Compare with the observed data in Fig. 2.

transient diabatic terms, along with computational inaccuracies as discussed for the momentum budget above.

Meridional cross-sections of contemporaneous correlations between model time tendency and forcing terms show similar magnitudes and spatial patterns to those for the observed data (Fig. 3). Tropical ($\partial\bar{u}/\partial t$) versus ($\hat{f}\overline{v*} + D_F$) correlations are somewhat stronger in the model than in observations, mainly due to increased correlation with $\hat{f}\overline{v*}$. Figure 5 shows a cross section of these correlations, which are positive and extend throughout the troposphere in low latitudes. Although the observations (Fig. 3c) show only a hint of such structure, these model results suggest that similar correlations may exist in the observed atmosphere if the data quantity were sufficient.

An important overall result is that there are relatively large equation residuals and less than perfect correlations in these calculations using daily sampled model data, even though the model data are sampled precisely. Because the observations have been assimilated with the use of a model similar overall to CCM1, it is unclear whether the analyzed residuals seen in Figs. 1 and 2 are due to computational inaccuracies, poor data and/or analyses, or unresolved momentum/thermodynamic sources and sinks.

4. Coherent wave–mean flow interactions

a. Observed data

Coherent variations among the various zonal mean variables are analyzed here via lag correlation analysis, allowing time lag information to be deduced along with spatially coherent structure in the meridional plane. The method used here is to choose one time series (in each hemisphere) as a reference for midlatitude wave amplitude variations; this reference time series is then used for correlating all other zonal mean variables. For the correlations shown here, the wave kinetic energy at 300 mb, averaged over 40°–50°, is chosen as the reference time series for each hemisphere. Kinetic energy was chosen simply for ease of calculation; one could also choose (for example) geopotential height variance or potential enstrophy for reference time series

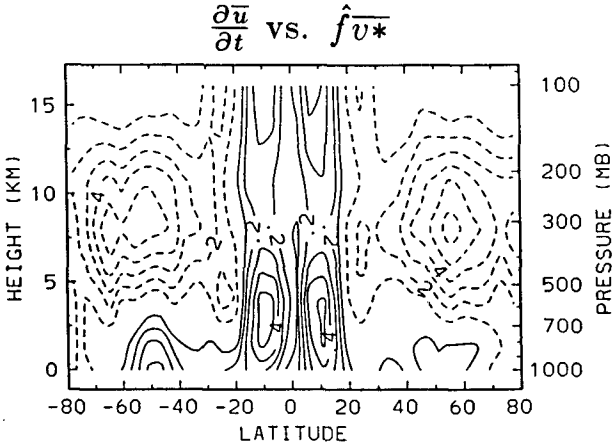

FIG. 5. Contemporaneous ($\partial\bar{u}/\partial t$) versus ($\hat{f}\overline{v*}$) correlation map for CCM1 data. Contours of ±0.1, 0.2, . . . ; compare with the correlation map for observed data in Fig. 3c.

as measures of wave variance; these other quantities were tested here, yielding nearly identical results to those shown below. The 40°–50° latitude reference position is chosen arbitrarily; the correlation patterns are not fixed geographically, and the structures observed here move with the choice of midlatitude reference position.

The correlation analyses are calculated separately for each hemisphere; the maps are then plotted on global meridional diagrams, allowing comparison between hemispheres. The time series are digitally filtered before calculating the correlations using a broad 3–25 day band-pass filter to "sharpen" the correlation diagrams (qualitatively similar results are found using the unfiltered time series); 3 and 25 day limits are chosen in light of power and cross-coherence spectra of the observed fluctuations that maximize in this range (not shown). The correlations were calculated separately

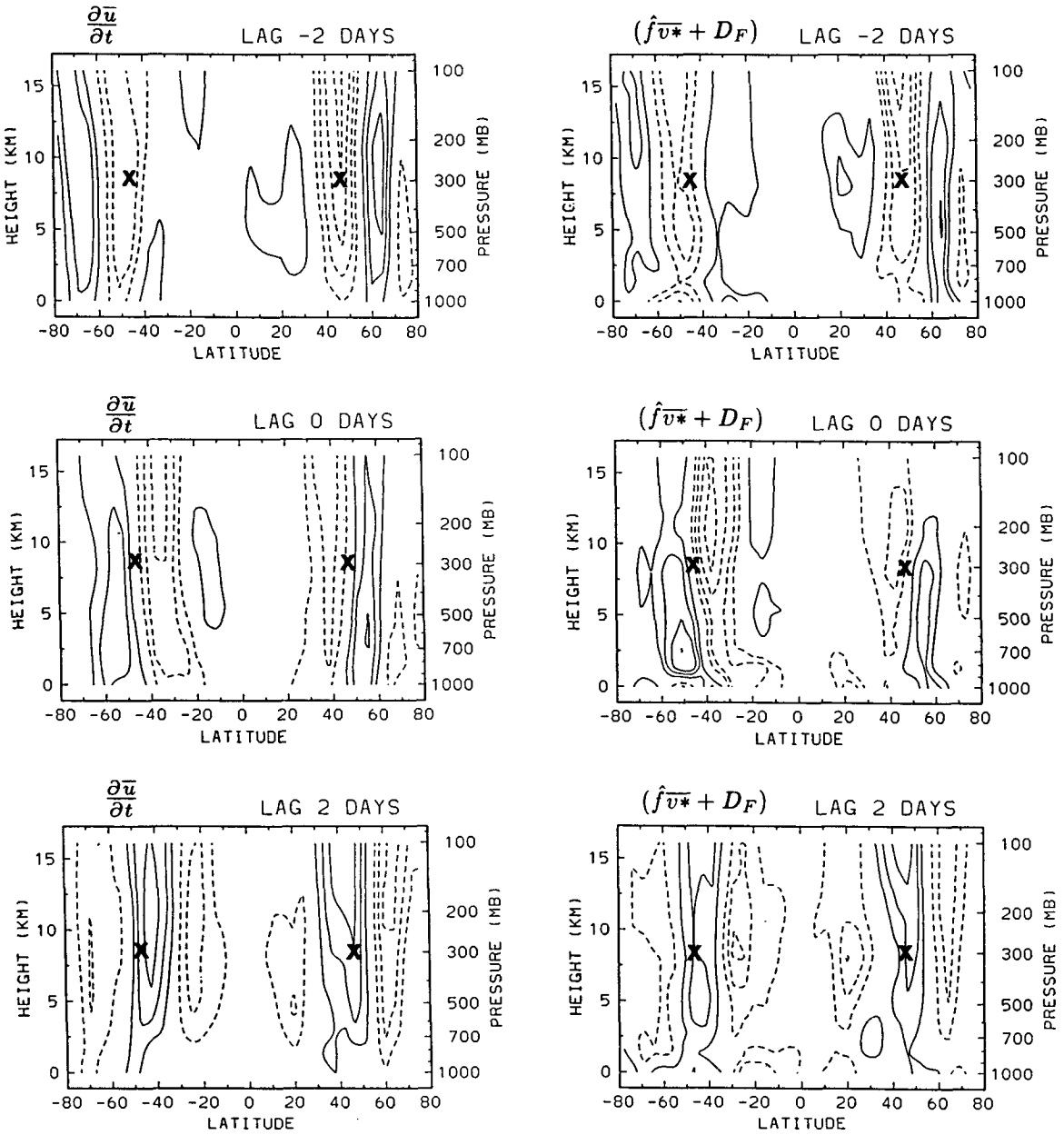

FIG. 6. Meridional cross-sections of correlations with respect to reference time series of wave kinetic energy at 300 mb, averaged over 40°–50° (denoted by the ×s). The correlations are calculated separately for each hemisphere, and plotted on global diagrams. Shown are $(\partial\bar{u}/\partial t)$ (left) and $(\hat{f}\overline{v^*} + D_F)$ (right) correlations, at time lags of −2 (top), 0 (middle), and +2 days (bottom). Contour interval of 0.05, with zero contours omitted.

for each of four 90-day seasons; because it was found that the results showed little seasonal dependence, correlation diagrams for all four seasons have been averaged together to produce a composite picture of wave–mean flow interactions. The patterns throughout this paper are very similar for NH and SH correlations, and the following discussion focuses on overall characteristics, without reference to a particular hemisphere (the fundamental nature of the dynamics observed here is emphasized by the NH–SH symmetry).

Figure 6 shows correlation diagrams, constructed as discussed above, for $(\partial\bar{u}/\partial t)$ and $(\hat{f}\overline{v^*} + D_F)$ variations. The correlation maps are shown for time lags of −2, 0, and +2 days; i.e., each time series is lagged with respect to the wave kinetic energy time series. The $\partial\bar{u}/\partial t$ correlations at lag −2 days in Fig. 6 show strong negative correlations (denoting decelerations) over 40°–50°, with weaker positive correlations (accelerations) flanking approximately 20° to the north and south. These correlations are in phase vertically, ex-

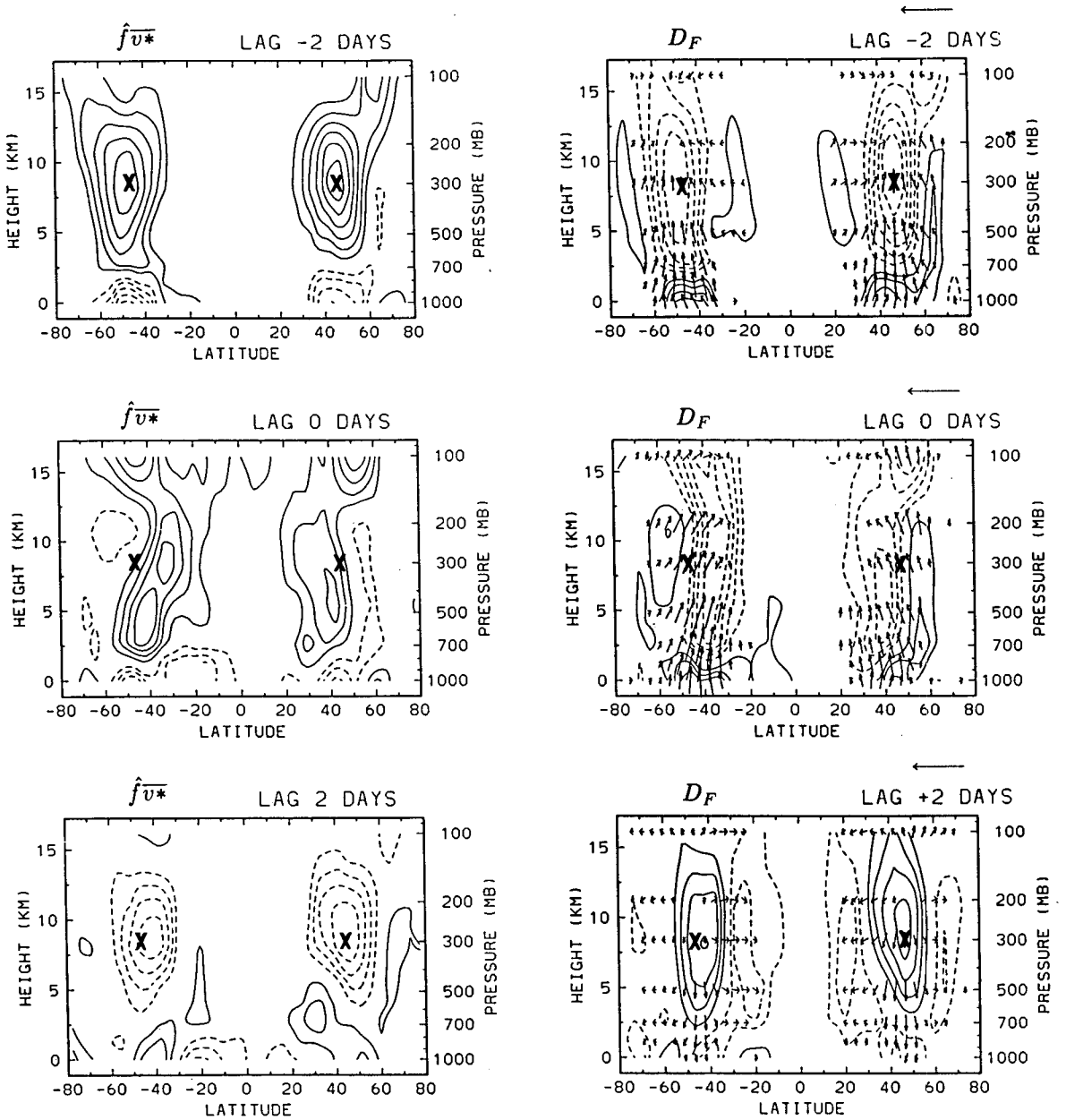

FIG. 7. Meridional cross-sections of correlations as in Fig. 6, but for $\hat{f}\overline{v^*}$ (left) and D_F (right) correlations separately. Contours as in Fig. 6. Also added in the right-hand panels are vectors denoting correlations with components of the EP flux vector, as described in the text.

tending throughout the entire troposphere. A nearly opposite structure is observed at lag +2 days, while the correlations at lag 0 show strong decelerations somewhat equatorward of those at lag −2 days.

The $(\hat{f}\overline{v^*} + D_F)$ correlation patterns in Fig. 6 are very similar to those of $(\partial\bar{u}/\partial t)$, with wavy meridional patterns and predominantly in-phase vertical structure. The good pointwise agreement in spatial and temporal patterns in Fig. 6 is consistent with the positive $(\partial\bar{u}/\partial t)$ versus $(\hat{f}\overline{v^*} + D_F)$ cross-correlation values observed throughout the meridional plane (Fig. 3a).

The $(\hat{f}\overline{v^*} + D_F)$ term in Eq. (1) represents the total mean flow acceleration; the direct wave driving is contained in the D_F term, while $\hat{f}\overline{v^*}$ is a secondary circulation that acts to mitigate D_F and redistribute the forcing in such a way as to maintain thermal wind balance (Dunkerton et al. 1981). The correlation patterns for the two separate terms $\hat{f}\overline{v^*}$ and D_F are shown in Fig. 7. Vectors in Fig. 7 denote correlations with the EP flux vector as discussed below. The central midlatitude $\hat{f}\overline{v^*}$ and D_F correlation patterns in Fig. 7 show nearly opposite spatial structures and evolution through time lags of −2 to +2 days; this demonstrates the mitigating effect of $\hat{f}\overline{v^*}$ on the central D_F maximum. Comparison between the D_F (Fig. 7) and $(\hat{f}\overline{v^*} + D_F)$ correlations (Fig. 6) shows the tendency for $\hat{f}\overline{v^*}$ to narrow the effective latitudinal scale of the forcing, and accentuate the wavy meridional structure. Vertical out-of-phase behavior is found for both $\hat{f}\overline{v^*}$ and D_F patterns above and below 700 mb in Fig. 7, but their combined influence is more nearly barotropic (Fig. 6). The central D_F maxima move equatorward and deepen vertically (into the lower stratosphere) over −2 to 0 days, while at +2 days the correlations are nearly opposite to those at −2 days. The equatorward D_F negative maxima (over 10°–30°) at +2 days are more pronounced than those in high latitudes.

The vectors in Fig. 7 represent correlations at each position with the separate components of the EP flux vector [Eq. (3b)]. The horizontal component measures correlation with F_ϕ, and likewise the vertical component with F_z; the reference arrow in the upper right-hand corner denotes a component correlation of 0.5 (the reference time series is still the 300 mb; 40°–50° kinetic energy). The evolution in Fig. 7 shows 1) the dominance of baroclinic processes (vertical arrows) during wave growth, and 2) vertical deepening and equatorward turning of $\vec{F}$ throughout the life cycle. Note that these correlations are all with respect to deviations from time mean values; the downward pointing arrows at lag +2 days denote a reduction in poleward heat flux (rather than absolute equatorward flux), as discussed further below.

Figure 8 shows similar correlation diagrams for $\partial\bar{T}/\partial t$, with vectors at each position denoting component correlations with the residual circulation components $\overline{v^*}$ and $\overline{w^*}$. The $\partial\bar{T}/\partial t$ patterns at −2 days show warming (positive correlations) over 1000–300 mb

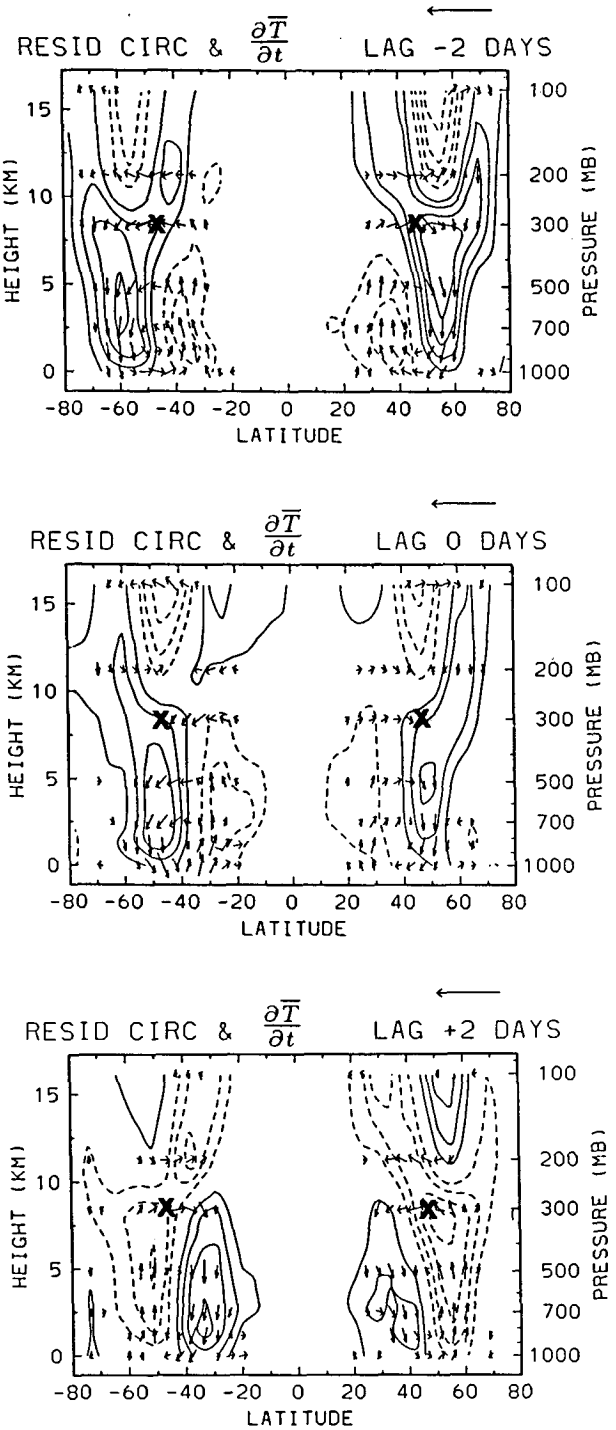

FIG. 8. Meridional cross-sections of $\partial\bar{T}/\partial t$ correlations, with vectors representing correlations with components of the residual circulation (see text for details).

centered near 50°–60°, with out-of-phase correlations (cooling) near 30°–40°. Vertical out-of-phase variations are seen above 200 mb, so that overall the $\partial\bar{T}/\partial t$ patterns exhibit a quadrupole structure in each

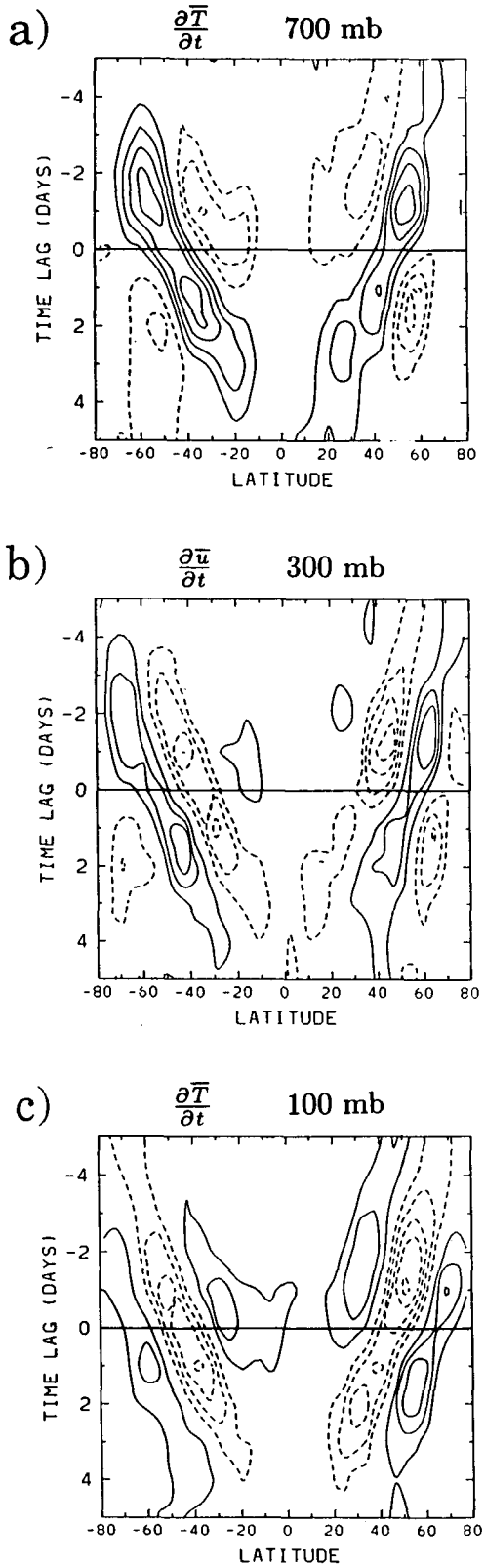

FIG. 9. Latitude–time lag sections of the correlations with wave kinetic energy time series at 300 mb, 40°–50° (calculated separately in each hemisphere) for (a) $\partial\bar{T}/\partial t$ at 700 mb, (b) $\partial\bar{u}/\partial t$ at 300 mb, and (c) $\partial\bar{T}/\partial t$ at 100 mb. Contour interval of 0.05, with zero contours omitted. Note the equatorward progression of these correlations with time in each hemisphere.

hemisphere. Note these $\partial\bar{T}/\partial t$ fluctuations are in thermal wind balance with the $\partial\bar{u}/\partial t$ patterns in Fig. 6; e.g., at lag −2 days the decrease in lower level temperature gradient implied in Fig. 8 is associated with a thermal wind deceleration in the middle and upper troposphere. The reversed $\partial\bar{T}/\partial t$ patterns above 200 mb act to reverse this thermal wind change above that level. The $\partial\bar{T}/\partial t$ patterns at lag +2 days are nearly opposite and identical to those at −2 days, while at lag 0 the correlations are similar to those at lag 0, but shifted ~10° equatorward.

Vector residual circulation correlation patterns in Fig. 8 show clear circulation cells below 200 mb in each hemisphere, with relative poleward flow in midlatitudes over 200–300 mb, upward motion near 40°, and downward motion near 60° at lag −2 days (reversed at lag +2 days). There is good agreement between observed $\partial\bar{T}/\partial t$ patterns and those implied by $\bar{w}^*$ vectors; i.e., rising $\bar{w}^*$ corresponding to local adiabatic cooling, and vice versa. This is consistent with the positive cross-correlations observed in midlatitudes in Fig. 3b. There are only weak hints in the $S\bar{w}^*$ correlations of reversed circulation cells above 300 mb, as suggested in the $\partial\bar{T}/\partial t$ patterns. These weak upper level patterns, together with the apparently excessive daily $S\bar{w}^*$ variance values (Fig. 2b) and lower cross correlations (Fig. 3b) above 300 mb, suggest that the $S\bar{w}^*$ values analyzed in the ECMWF data above 300 mb are excessively noisy.

To illustrate the time development of the correlations more concisely, Fig. 9 shows latitude–time lag plots of the correlations of $\partial\bar{T}/\partial t$ at 700 and 100 mb, and $\partial\bar{u}/\partial t$ at 300 mb. These figures show that the strongest zonal mean flow changes occur on the order of 1–2 days prior to and following wave energy maxima; this gives an estimate of the time scale of wave growth and decay for individual events. Figure 9 also reiterates the vertical out-of-phase $\partial\bar{T}/\partial t$ variations (compare Figs. 9a–c) and the thermal wind balance between $\partial\bar{T}/\partial t$ and $\partial\bar{u}/\partial t$. Note that the zonal temperature and wind changes in Fig. 9 show clear tendencies to propagate equatorward in time with a speed near 7° latitude per day (or 10 m s^{-1}).

Figure 10 shows similar diagrams for heat and momentum flux and EP flux divergence correlations—here the signs of the heat and momentum flux correlations have been reversed in the SH so that positive correlations are associated with poleward fluxes (thus the NH and SH patterns are symmetric). Strong poleward fluxes of heat are seen in midlatitudes at 700 mb 0–2 days prior to upper tropospheric wave maxima (Fig. 10a), consistent with baroclinic growth of the waves. Somewhat weaker negative correlations are seen

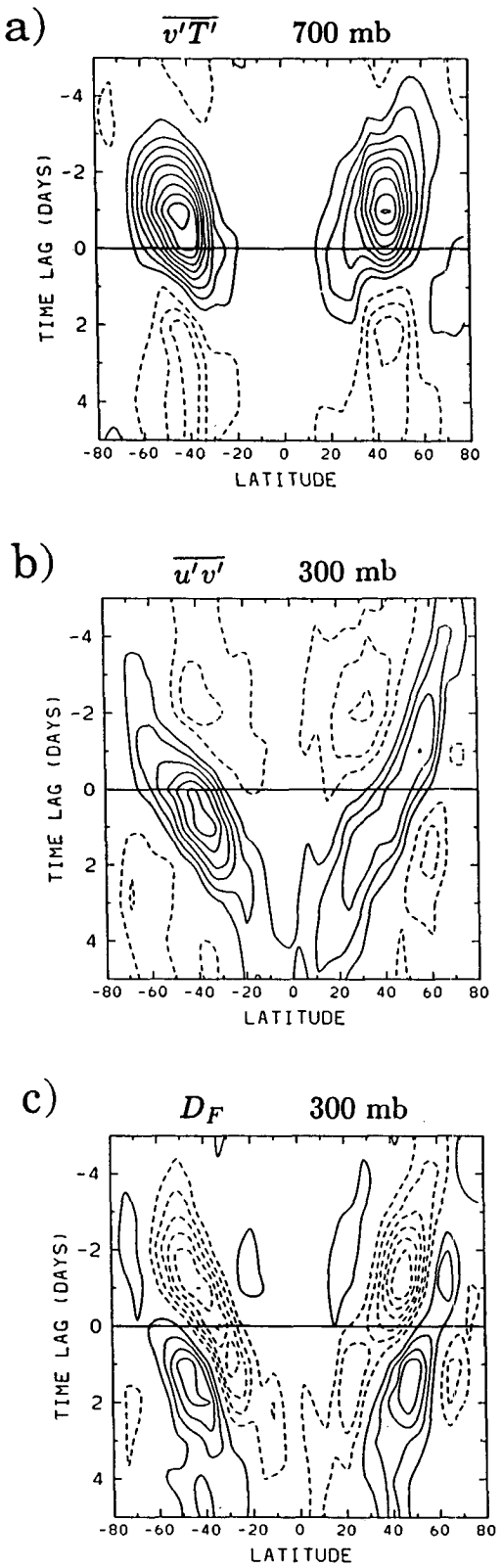

FIG. 10. Latitude–time lag correlation sections as in Fig. 9, but for (a) poleward heat flux at 700 mb, (b) poleward momentum flux at 300 mb, and (c) D_F variations at 300 mb. The sign of the SH correlations in (a) and (b) have been reversed, so that positive correlations denote poleward fluxes (to by symmetric with the NH correlations).

near lags of +2 to +3 days. Because the heat flux daily standard deviations at 700 mb are less than the time average values (not shown here), the negative correlations at positive time lag in Fig. 9a do not imply absolute equatorward heat flux, but rather a reduction in poleward transport.

Momentum flux correlations at 300 mb in Fig. 10b show poleward flux (positive contours) in midlatitudes at lags of zero to +2 days, consistent with the strong equatorward EP flux vectors observed during the barotropic decay phase of baroclinic wave life-cycles (Edmon et al. 1980; Hoskins 1983; Randel and Stanford 1985). There is a clear tendency for the correlation maxima to move equatorward in time, with significant values reaching into the tropics at lags +2 to +4 days. A somewhat surprising finding is that negative momentum flux correlations occur in middle latitudes 2–3 days *prior* to wave variance maxima, and ~1 day prior to the strongest low level heat fluxes (Fig. 9a). As with the heat flux variations discussed above, these correlations denote a reduction in the poleward flux (a decrease in meridional tilt of the waves) at this time rather than an actual equatorward flux. The EP flux divergence correlations (Fig. 10c) show good qualitative agreement with the $\partial\bar{u}/\partial t$ correlations in Fig. 9b, while similar ($\hat{f}\overline{v^*} + D_F$) patterns (not shown) show nearly exact agreement with all details seen in the $\partial\bar{u}/\partial t$ correlations. Figure 9c also clearly shows the tropical influence of waves with midlatitude origins.

Linear theory predicts that local wave potential enstrophy ($\frac{1}{2}\overline{q'^2}$) tendencies should follow patterns of wave driving D_F according to

$$\partial/\partial t\left(\frac{1}{2}\overline{q'^2}/\bar{q}_y\right) = -D_F, \qquad (5)$$

where $\bar{q}_y$ is the background potential vorticity gradient (Edmon et al. 1980). Noting that $D_F = \overline{v'q'}$, this equation is a linear flux-gradient equation for quasi-geostrophic potential vorticity (q'). To demonstrate this relationship qualitatively in these data, correlations are calculated between (i) kinetic energy *tendency* (which should behave similarly to potential enstrophy tendency—note $\bar{q}_y$ variations were tested and found to be insignificant in Eq. 5), and (ii) reference time series of 700 mb, 40°–50° poleward heat flux. This choice of reference time series is made because the heat flux–wave energy correlations are strong and peaked rather sharply in time (see Fig. 10a). Note that the heat flux peaks ~1 day prior to the 300 mb energy maxima (see Fig. 10a), and this one day needs to be subtracted from the time lags to make the correlations approximately comparable to all the previous diagrams.

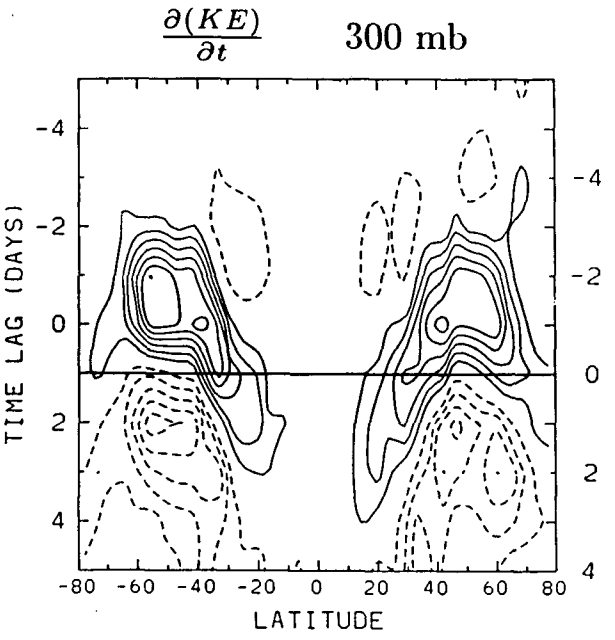

FIG. 11. Latitude–time lag sections at 300 mb of correlations between wave kinetic energy tendency and reference time series of $\overline{v'T'}$ at 700 mb, 40°–50° (made separately for each hemisphere). Positive correlations denote local wave growth, negative contours denote wave decay. The modified time lags on the right axes can be used to approximately compare with the previous correlation diagrams (see text for details). Note the meridional spreading of the tendency correlations in each hemisphere, particularly towards low latitudes.

Figure 11 shows a latitude–time lag diagram of these correlations at 300 mb; this diagram shows local wave growth/decay regions associated with low level poleward heat flux; note the modified time lags added on the right-hand axes in Fig. 11. Strong positive correlations are seen over 40°–60° at (modified) lags −1 to −2 days in Fig. 11, denoting local wave growth, while the midlatitude negative correlations over +1 to +2 days show local wave decay. The important point of these patterns is that they reveal clear meridional spreading of the wave activity tendency, particularly towards lower latitudes, in good qualitative agreement with the D_F development in Fig. 10c. Very similar behavior is obtained for the idealized barotropic decay calculations in Held and Hoskins (1985, their Fig. 6) and Held and Phillips (1987, their Fig. 2), which are based on the barotropic equivalent to Eq. (5).

Figure 12 shows dimensionalized EP flux diagrams constructed to represent a sort of composite life cycle. These diagrams are constructed as follows: dimensional values are assigned the separate $\overline{v'T'}$, $\overline{u'v'}$, and D_F correlation values previously shown by equating the largest correlations (at any time lag) with a value of twice the daily standard deviation. The correlations are weighted by the square root of the cos(latitude) to account for the increase of variance with latitude of zonal mean quantities, as discussed in section 3. These dimensional values at each time lag are then added to the time (annual) means of each quantity to produce the signatures in Fig. 12. The intention here is simply to depict realistic variations throughout a life cycle, including the time-mean values.

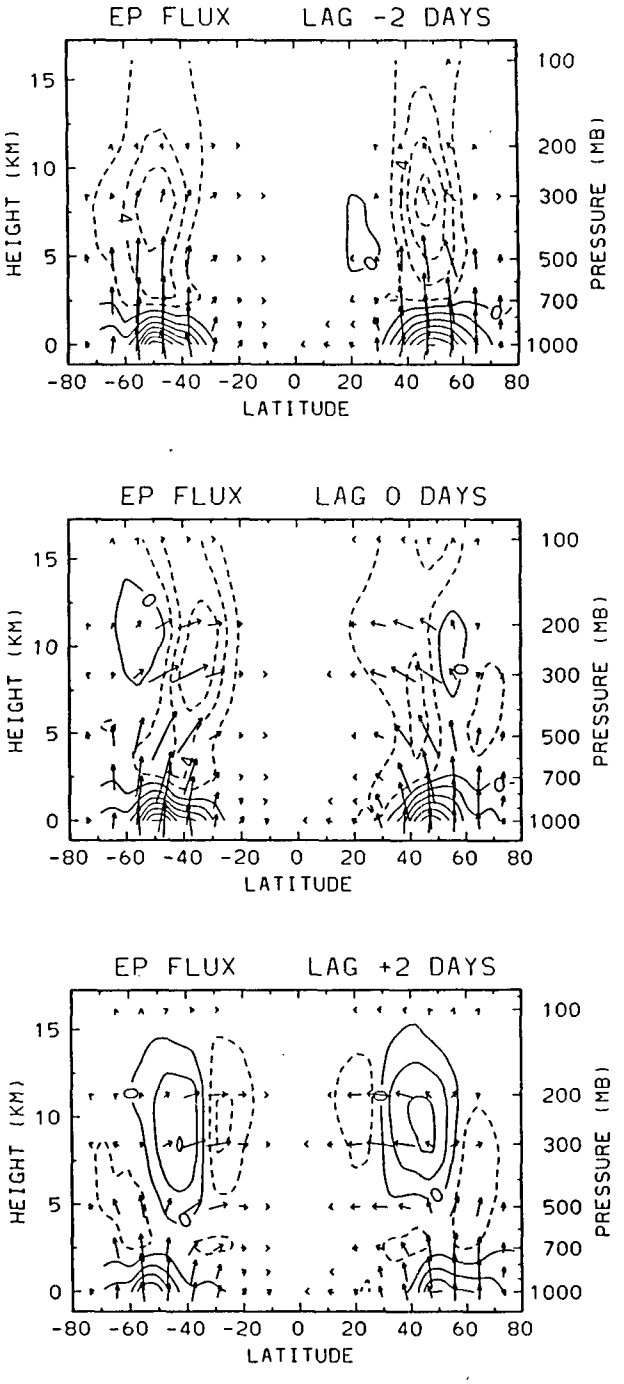

FIG. 12. Dimensional (composite) EP flux diagrams constructed from the cross-correlation values, daily standard deviation fields, and time-mean values (as described in text). Vectors use standard scaling, and contours are of D_F, with contour interval of 2 m s^{-1} day^{-1}.

The structure during wave growth (lag −2 days) is almost entirely baroclinic, with upper level poleward momentum fluxes reduced compared to time-mean values. Barotropic processes become dominant in the upper levels during maturity and decay, and there is a reversal in sign of D_F in the midlatitude upper troposphere. Associated with this change of sign is a local loss of midlatitude wave activity via propagation to low latitudes. Note the heat fluxes in low levels are always poleward.

Furthermore, the correlations here reveal fluctuations in the Eulerian mean meridional circulations directly associated with wave growth and decay. Figure 13a shows wave correlations with the Eulerian mean meridional circulations ($\bar{v}$ and $\bar{w}$) in a vector correlation diagram, similar to those in Fig. 8 (again using wave energy at 300 mb, 40°–50° as reference). These vectors show a clear indirect circulation cell in midlatitudes of each hemisphere, with rising motion in high latitudes (60°), sinking near 40°, equatorward flow at and above 300 mb, and poleward flow in low levels (700 and 850 mb). These correlations are direct evidence of large-scale wave modulation of the Ferrel cells. The Eulerian-mean circulation in Fig. 13a is oppositely directed to the TEM residual circulation in Fig. 8b, demonstrating the predominant effect (with opposite sign) of the $\overline{v'T'}$ terms in Eqs. (4a) and (4b). *Wave-induced Eulerian-mean motions in these observations are thus opposed to (and less than) the direct eddy flux divergence terms* in Eqs. (4a) and (4b). This is exactly the sense of the meridional circulation anticipated from localized heat flux variations and incorporated into the TEM theory.

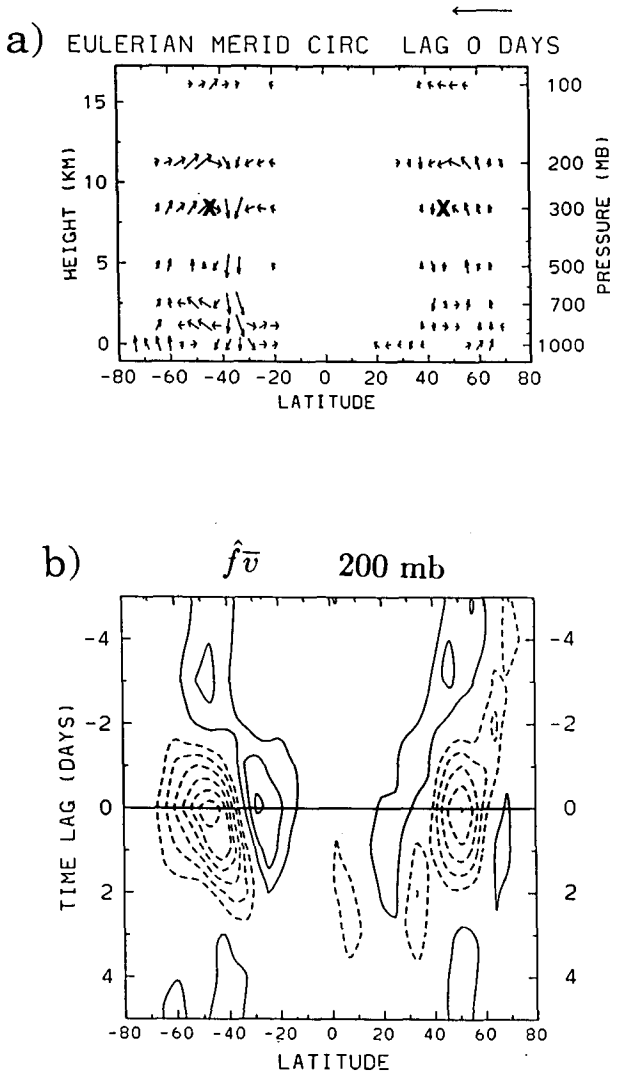

FIG. 13. (a) Vectors denoting correlations between wave kinetic energy time series and components of the Eulerian mean circulation ($\bar{w}$ and $\bar{v}$), at zero lag time, calculated similarly to those in Fig. 8. The reference vector in the right-hand corner denotes a component correlation of 0.5 (b) Latitude–time lag section of the correlation of $\hat{fv}$, showing the time development of the 200 mb correlations in (a).

Figure 13b shows time-lag development of the 200 mb $\bar{v}$ correlations, which are strongest near lag 0 (i.e., coincident with wave energy maxima); similar behavior is found of 500 mb $\bar{w}$ correlations. Because $\overline{v'T'}$ correlations are strongly asymmetric with respect to wave energy (Fig. 10a), this shows that the Eulerian-mean circulation does not respond to $\overline{v'T'}$ variations alone (in which case both correlations would be identically timed), but rather to *both* eddy heat and momentum flux divergence variations (as should be expected).

b. Corroboration in general circulation model results

Analysis of results from a general circulation model (GCM) is included here to corroborate the observational data analyses shown above. Overall the cross-correlation results are nearly identical to those seen in observed data, and only selected comparisons are shown here.

Figures 14a and 14b show 300 mb latitude–time lag sections of kinetic energy correlations with $\partial\bar{u}/\partial t$ and D_F for CCM1, for comparison with the observed patterns in Figs. 9b and 10c, respectively. The model correlations show the same overall character of wavy meridional structures and reversibility between wave growth and decay. The model correlations for both variables exhibit less continuous equatorward propagation than that seen in observations, and furthermore do not extend to as low latitudes as those observed. These differences may be related to the lack of transient eddy poleward momentum flux in midlatitudes in CCM1, as discussed in Randel and Williamson (1989). This lack of model momentum flux is consistent with a reduction in equatorward wave propagation, as evidenced in these correlations.

Figure 15 shows dimensional EP flux diagrams for CCM1, constructed in an identical manner to those for the observations in Fig. 12. Note that the CCM

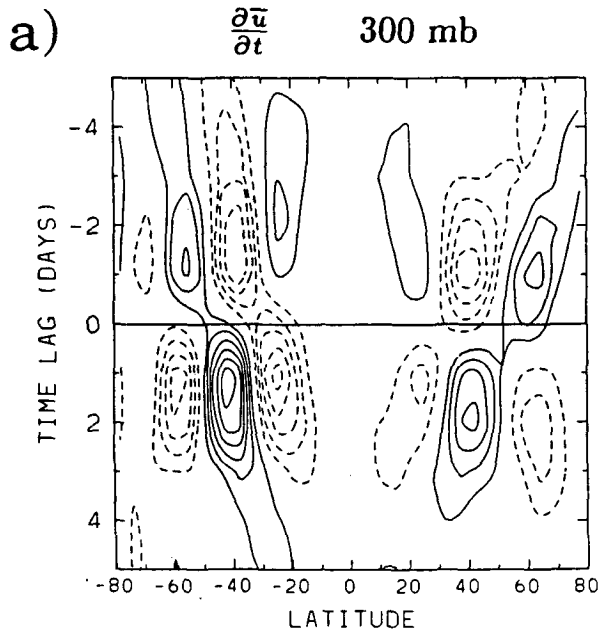

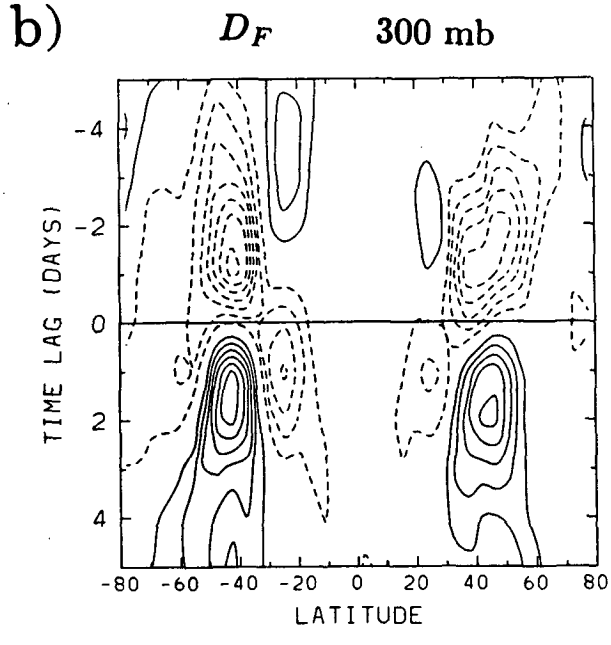

FIG. 14. Latitude–time lag correlations between wave kinetic energy and (a) 300 mb $\partial\bar{u}/\partial t$, and (b) 300 mb D_F, calculated from CCM1 data. Correlations from observations are shown in Figs. 9b and 10c, respectively.

calculations are only made above the 850 mb level. Time-mean EP flux signatures for both observations and model are shown in Randel and Williamson (1989). The overall life cycle evolution revealed here is very similar between modeled and observed data. The lag 0 patterns are somewhat different, with the model D_F showing less equatorward propagation than that observed. As discussed above, this is due to the lack of model transient eddy momentum flux, as evidenced by comparing the horizontal vector components in Figs. 12 and 15 in the upper troposphere at lags 0 and +2 days.

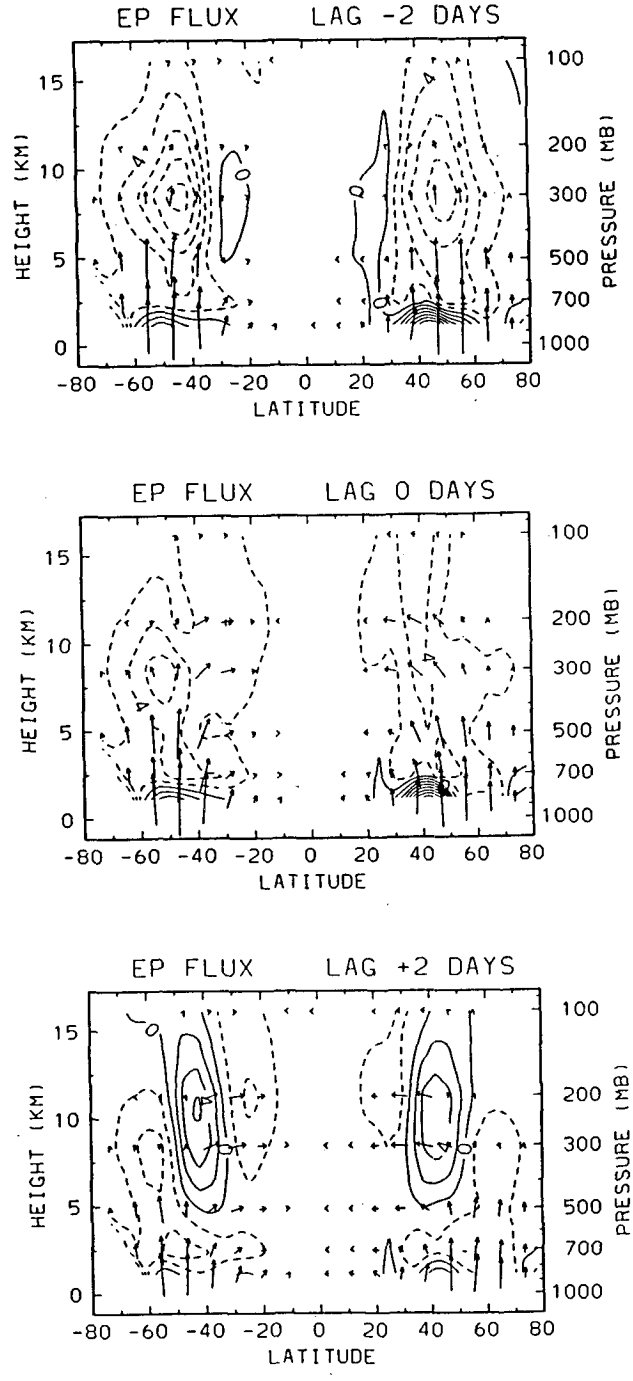

FIG. 15. Dimensional EP flux diagrams for CCM1, calculated identically to those from observed data (Fig. 12).

5. Case study

A particular case study of a large amplitude wave–mean flow interaction event is described here to reinforce the correlation analyses and illustrate the differences that can be evident with any particular event. The case is similar in many aspects to the baroclinic wave life cycle in the SH summer analyzed by Randel and Stanford (1985); the main addition here is that the associated meridional circulations are also analyzed. The particular event is chosen from the latitude–time cross section of zonal mean wind, and time series of poleward eddy heat flux and EP flux divergence for 1984 (shown in Fig. 16). The $\overline{v'T'}$ and D_F plots (Fig. 16b) illustrate the episodic nature of wave events with a time scale of order 10 days. This event is in the NH during October, as marked by the arrows in Fig. 16, and was chosen for no other reason than its relatively large amplitude.

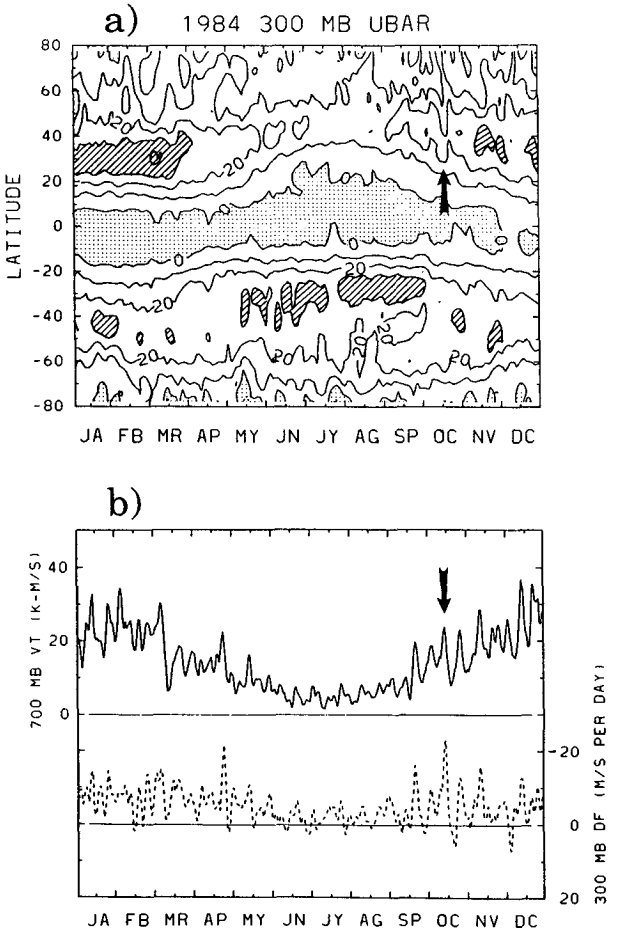

FIG. 16. (a) Latitude–time section of zonal mean zonal wind during January–December 1984; contours of 10 m s^{-1}. (b) Time series of 700 mb poleward eddy heat flux (solid line, left ordinate) and 300 mb EP flux divergence (dashed line, right ordinate), averaged over 30°–60°N. The case study analyzed here is indicated by the arrow in each panel.

Figure 17 shows polar stereographic plots of the 300 mb geopotential throughout this life cycle. Very intense development is seen between 13–16 October; the low level poleward heat flux peaks on 15 October. Wave amplitudes are largest over 16–18 October, culminating with a separation of the two lows near 110° and 170°W from the main vortex (Fig. 17c). The hemispheric patterns return to a more normal situation by 20 October (Fig. 17d) as the wave amplitudes decrease. Quasi-stationary zonal waves 4–6 dominate the wave spectra throughout this event.

Wave–mean flow diagnostics are analyzed by taking 3-day means prior to and subsequent to wave amplitude maxima: 14–16 October and 18–20 October, respectively (referred to hereafter as pre- and postmaximum means). Both 0000 and 1200 UTC ECMWF analyses are used in the 3-day averages.

Figure 18 shows meridional cross-sections of $\partial\bar{u}/\partial t$, EP flux cross sections, and $\partial\bar{T}/\partial t$-vector residual circulation diagrams for the pre- and postmaximum averages. The $\partial\bar{u}/\partial t$ and D_F contours in Fig. 18 have been multiplied by cos(latitude). The premaximum $\partial\bar{u}/\partial t$ (Fig. 18) shows deceleration over 50°–60°, peaking near -1 m s^{-1} per day, with weaker acceleration regions flanking approximately 15° to the north and south. The premaximum EP flux diagram (Fig. 18b) shows strong heat flux in low levels over 40°–60°, with strong flux convergence (maximum -10 m s^{-1} per day) in the upper troposphere. There are weak regions of positive D_F poleward and equatorward of the central negative D_F maximum. The $\hat{f}\overline{v}^*$ acceleration (not shown) has a pattern similar to and opposite that of D_F in Fig. 18b, with a central maximum near 6 m s^{-1} per day; the analyzed residual of Eq. (1) (not shown) has maxima of order 1 m s^{-1} per day; of the same sign and slightly larger than the observed $\partial\bar{u}/\partial t$.

Figure 18c shows components of the residual circulation plotted as vectors in the meridional plane; the arrows are drawn such that they represent the net parcel displacements that would occur over three days. Strong midlatitude poleward flow centered near 300 mb is seen in this diagram, consistent with the $\hat{f}\overline{v}^*$ acceleration discussed above. The overall patterns show a clockwise circulation cell over 1000–300 mb, with hints of a weaker one of opposite polarity above 300 mb. The observed $\partial\bar{T}/\partial t$ patterns are also added in this diagram, showing good qualitative agreement with observed $\overline{w}^*$ vectors; i.e., a quadrupole pattern in midlatitudes. However, the zonal temperature tendency estimated from $S\overline{w}^*$ is more than twice as large as that observed, and there is a large residual to Eq. (2).

The postmaximum averages shown in Fig. 18 show primarily a reversal of the premaximum patterns. The zonal wind exhibits acceleration over 50°–60°, flanked by deceleration regions. The EP flux diagram shows positive divergence in the midlatitude upper troposphere, and negative patterns to the north and south. The low level heat flux has decreased markedly from

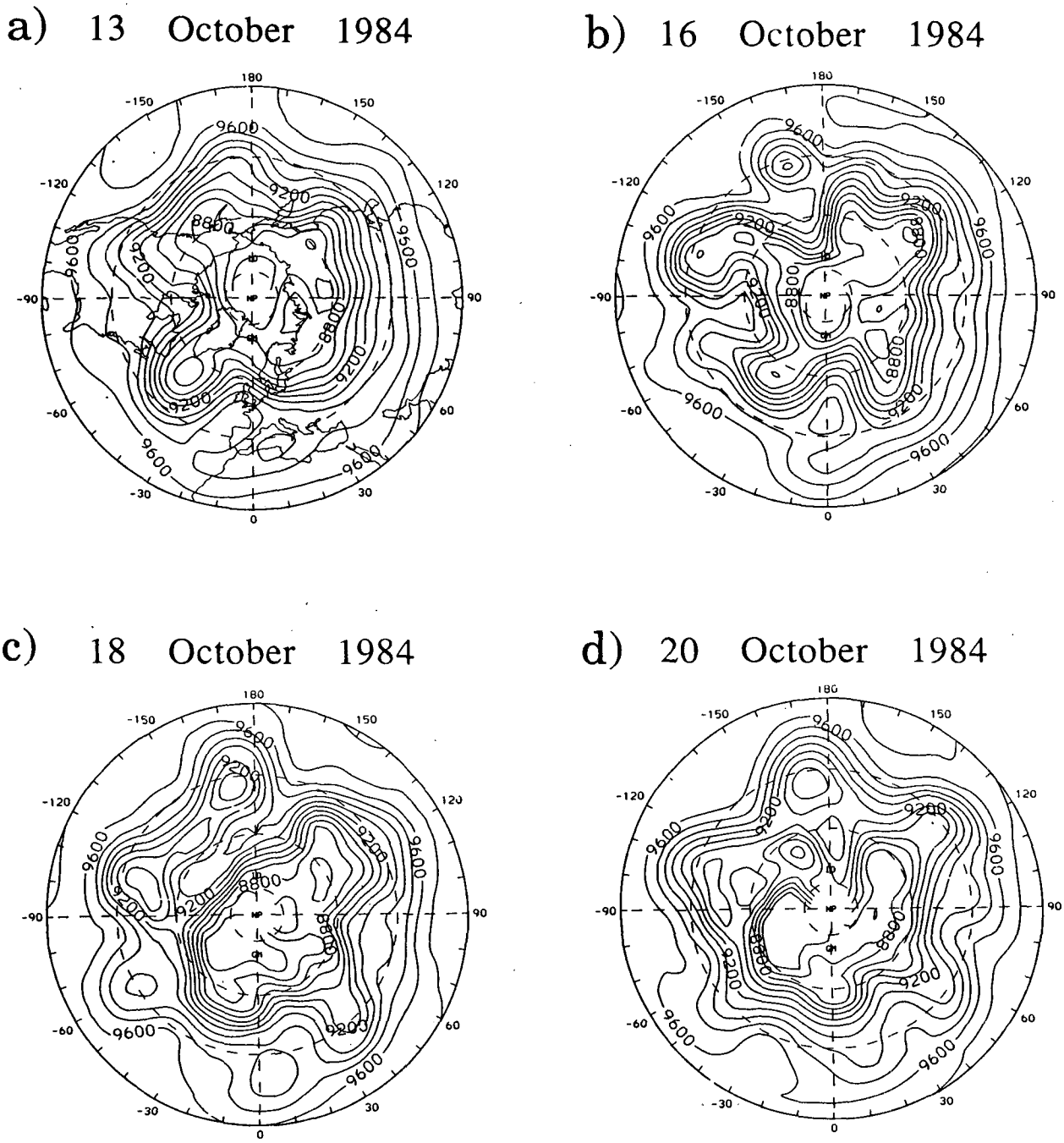

FIG. 17. Northern Hemisphere polar stereographic projections of the 300 mb geopotential height contours during wave growth/decay event case study, 13–20 October 1984. Geographic outlines are added in (a).

the premaximum average, although it is still poleward. The $\hat{f}\overline{v}^*$ acceleration again primarily balances D_F, with Eq. (1) residuals somewhat larger than observed $\partial\bar{u}/\partial t$.

The postmaximum residual circulation (Fig. 18f) shows less coherent structure than the premaximum average, but there is an overall reversal of the high latitude patterns in Fig. 18c, in qualitative agreement with the observed $\partial\bar{T}/\partial t$ contours. Postmaximum Eq. (2) residuals are again of order twice the observed $\partial\bar{T}/\partial t$.

6. Summary and discussions

Daily balances in the zonally averaged tropospheric flow have been analyzed here by (i) comparing daily rms equation residuals to rms values of the individual terms, and (ii) correlating observed time tendencies to

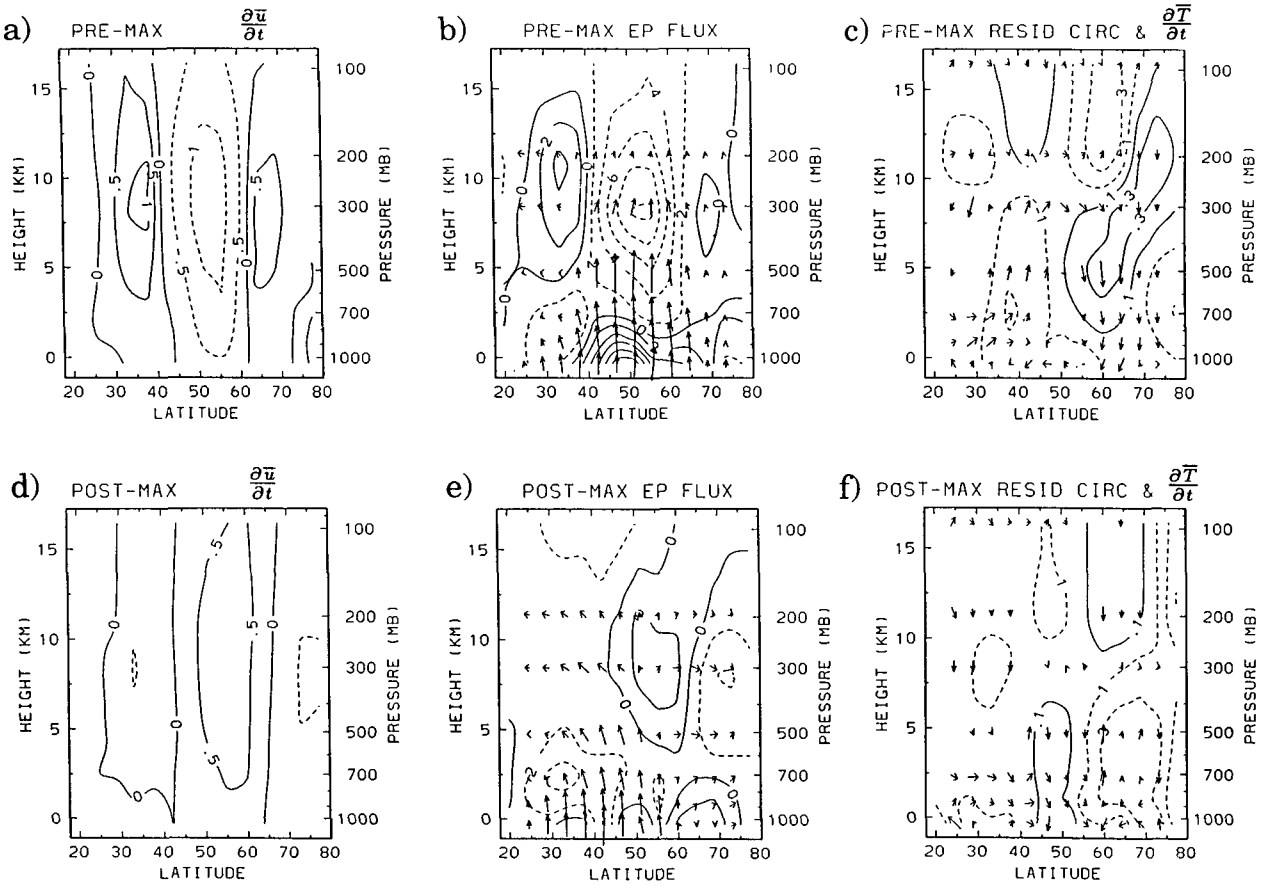

FIG. 18. Premaximum (top) and postmaximum (bottom) 3-day average meridional cross-sections during case study. Shown are (left) observed $\partial\bar{u}/\partial t$ (contours of 0.5 m s^{-1} day^{-1}), (middle) EP flux diagrams (the vectors use standard scaling, and contours are 2 m s^{-1} day^{-1}), and (right) residual circulation vector diagrams with observed $\partial\bar{T}/\partial t$ (K day^{-1}). The residual circulation vectors (right) are drawn so that their lengths indicate net displacement that would occur in three days.

observed forcing terms. The observed zonal mean wind and temperature tendencies both show strong correlations with values anticipated via Eqs. (1) and (2) throughout much of the extratropical troposphere (away from the surface). Tropical zonal wind tendency fluctuations are coherent with those anticipated from quasi-geostrophic wave driving, while tropical temperature tendencies are incoherent with analyzed zonal mean vertical velocities. This latter statement holds even for 1986, when ECMWF analyses of the Hadley circulation were improved substantially over prior years (see Trenberth and Olson 1988). Zonal wind equation residuals are of the same order as observed $\partial\bar{u}/\partial t$ values, suggesting daily tendencies can only be estimated to within a factor of 2. Zonal temperature equation residuals are substantially larger than observed tendencies, showing little hope of quantitatively estimating $\partial\bar{T}/\partial t$ values. This is particularly true above 500 mb, likely due to poor analyses of mean meridional circulations above this level. Overall similar results are seen in analyses of GCM data. Momentum and thermodynamic residuals in the model data are due to calculational inaccuracies and sampling biases (as discussed in section 4b), while thermodynamic residuals have contributions from parameterized diabatic terms.

The evolving signatures of baroclinic wave life-cycles and their influences on the mean flow have been revealed here via cross-correlation analyses, including coherent fluctuations in zonal mean temperature, three-dimensional winds, and quadratic wave quantities. Observed zonal wind tendency variations are nearly barotropic throughout 1000–100 mb, and exhibit meridional out-of-phase behavior with a half-wavelength near 15° latitude. Kidson (1988) has noted similar structure for synoptic time scale zonal wind fluctuations in a 15-year sample of Australian analyses; somewhat longer meridional scales were observed for lower frequency fluctuations. Quadrupole variations in $\partial\bar{T}/\partial t$ are observed here, with vertical and meridional out-of-phase correlation maxima (in thermal wind balance with $\partial\bar{u}/\partial t$ variations); these fundamental patterns of variability are also revealed by empirical orthogonal function (EOF) analyses (not shown here). These $\partial\bar{u}/\partial t$ and $\partial\bar{T}/\partial t$ patterns are in good agreement with those anticipated due to localized forcing of a balanced symmetric vortex; see for example the temper-

ature tendency patterns in Garcia (1987; his Fig. 12). Similarly, the residual circulations observed here are in good agreement with those anticipated for localized forcing (Eliassen 1951; Dunkerton et al. 1981; Garcia 1987; his Figs. 11 and 14). However, in spite of these good qualitative agreements, the maximum contemporaneous correlations are only of order 0.5–0.6 (i.e., 25–35 percent linearly dependent variance), even for "perfectly" sampled GCM data. There are thus substantial limitations to the quantitative application of adiabatic, zonal mean theory to observed tropospheric variations.

The correlation analyses here reveal that poleward heat flux correlations (which are strongly positive prior to wave variance maxima, demonstrating baroclinic wave growth) are negative during wave decay; these negative correlations result from a systematic decrease in poleward heat flux this time rather than actual equatorward flux. Strong poleward momentum fluxes are observed coincident with and subsequent to wave variance maxima (i.e., barotropic decay of the waves); a new finding here is the negative correlations several days *prior* to wave amplitude maxima. These correlations result from a decrease in the poleward flux during this time; i.e., *the waves exhibit small meridional phase tilts just prior to their largest baroclinic growth.* Clear meridional propagation of midlatitude wave activity (Rossby wave radiation) is observed; momentum flux and zonal wind tendency variations can be traced deep into the tropics.

An interesting aspect of all the correlations shown here is the degree of symmetric reversibility between wave growth and decay phases (most of the patterns in Figs. 6–8 are reversed between lags of −2 and +2 days). This aspect is very reminiscent of the wave amplitude vacillations obtained by Thompson (1987) as the response to differential heating in an idealized two level, quasi-geostrophic model. Thompson's model produces regular wave amplitude vacillations due solely to baroclinic wave–mean flow interactions; in particular, positive and negative poleward eddy heat variations (about the time-mean value; the net heat fluxes are poleward at any instant). The positive and negative heat flux correlations (Fig. 10a) suggest that one might view the coherent fluctuation in zonal means observed here in a qualitatively similar manner to Thompson's simple model results (although barotropic effects, which are neglected by Thompson, are certainly also important here). Note that although such reversibility can be suggestive of linear behavior, Thompson's vacillations are fundamentally nonlinear.

Acknowledgments. The author thanks Drs. Kevin Trenberth, Roland Madden, and Roland Garcia for discussions and comments on an earlier version of this manuscript. Walter Robinson and an anonymous reviewer provided constructive comments that improved the presentation of these results. Dorene Howard expertly typed the manuscript through several revisions. The data analyzed here was provided by ECMWF. Dr. John Kidson supplied the computer code for access to the ECMWF zonal mean data. This work has been partially supported by NASA Grant W16215.

REFERENCES

Andrews, D. G., and M. E. McIntyre, 1976: Planetary waves in horizontal and vertical shear: The generalized Eliassen–Palm relation and the mean zonal acceleration. *J. Atmos. Sci.*, **33**, 2031–2048.

Baldwin, M. P., H. J. Edmon, Jr. and J. R. Holton, 1985: A diagnostic study of eddy-mean flow interactions during FGGE-SOP1. *J. Atmos. Sci.*, **42**, 1838–1845.

Boyd, J. P., 1976: The noninteraction of waves with the zonally averaged flow on a spherical earth and the interrelationships of energy, heat and momentum. *J. Atmos. Sci.*, **33**, 2285–2291.

Dunkerton, T. J., C.-P. F. Hsu and M. E. McIntyre, 1981: Some Eulerian and Lagrangian diagnostics for a model stratospheric warming. *J. Atmos. Sci.*, **38**, 819–843.

Edmon, H. J., Jr., B. J. Hoskins and M. E. McIntyre, 1980: Eliassen–Palm cross sections for the troposphere. *J. Atmos. Sci.*, **37**, 2600–2616; also Corrigendum, *J. Atmos. Sci.*, **38**, 1115 (1981).

Eliassen, A., 1951: Slow thermally or frictionally controlled meridional circulation in a circular vortex. *Astrophys. Norv.*, **5**, 19–60.

Garcia, R. R., 1987: On the mean meridional circulation of the middle atmosphere. *J. Atmos. Sci.*, **44**, 3599–3609.

Held, I. M., and B. J. Hoskins, 1985: Large-scale eddies and the general circulation of the troposphere. *Advances in Geophysics*, **28A**, 3–31.

——, and P. J. Phillips, 1987: Linear and nonlinear barotropic decay on the sphere. *J. Atmos. Sci.*, **44**, 200–207.

Hoskins, B. J., 1983: Modelling of the transient eddies and their feedback on the mean flow. *Large-Scale Dynamical Processes in the Atmosphere*, B. J. Hoskins and R. P. Pearce, Eds., Academic Press, 397 pp.

Kidson, J. W., 1988: Indices of the Southern Hemisphere zonal wind. *J. Climate*, **1**, 183–194.

Lau, K.-M., and D. H. Chan, 1983: Short-term climate variability and atmospheric teleconnections from satellite-observed outgoing longwave radiation. Part II: Lagged correlations. *J. Atmos. Sci.*, **40**, 2751–2767.

North, G. R., F. J. Moeng, T. L. Bell and R. F. Calahan, 1982: The latitude dependence of the variance of zonally averaged quantities. *Mon. Wea. Rev.*, **110**, 319–326.

Pfeffer, R. L., 1987: Comparison of conventional and transformed Eulerian diagnostics in the troposphere. *Quart J. Roy. Meteor. Soc.*, **113**, 237–254.

Randel, W. J., and J. L. Stanford, 1985: The observed life cycle of a baroclinic instability. *J. Atmos. Sci.*, **42**, 1364–1373.

——, and D. L. Williamson, 1989: Comparison of the climate simulated by the NCAR Community Climate Model (CCM1:R15) with ECMWF analyses. *J. Climate*, in press.

Simmons, A. J., and B. J. Hoskins, 1978: The life cycles of some nonlinear baroclinic waves. *J. Atmos Sci.*, **35**, 414–432.

Thompson, P. D., 1987: Large-scale dynamical response to differential heating: Statistical equilibrium states and amplitude vacillation. *J. Atmos. Sci.*, **44**, 1237–1248.

Trenberth, K. E., 1987: The role of eddies in maintaining the westerlies in the Southern Hemisphere winter. *J. Atmos. Sci.*, **44**, 1498–1508.

——, and J. G. Olson, 1988: An evaluation and intercomparison of global analyses from the National Meteorological Center and the European Centre for Medium Range Weather Forecasts. *Bull. Amer. Meteor. Soc.*, **69**, 1047–1057.